Title

Simultaneous quantitative susceptibility mapping (QSM) and for high iron concentration quantification with 3D ultrashort echo time sequences: An echo dependence study

Journal

Magnetic Resonance in Medicine, 79(4)

ISSN

0740-3194

Authors

Lu, Xing
Ma, Yajun
Chang, Eric Y
et al.

Publication Date

2018-04-01

DOI

10.1002/mrm.27062

Peer reviewed

BIOPHYSICS AND BASIC BIOMEDICAL RESEARCH – Rapid Communication

Magnetic Resonance in Medicine 79:2315–2322 (2018)

Simultaneous Quantitative Susceptibility Mapping (QSM) and R_2^* for High Iron Concentration Quantification With 3D Ultrashort Echo Time Sequences: An Echo Dependence Study

Xing Lu,[1,2] Yajun Ma,[1] Eric Y. Chang,[1,3] Qun He,[1] Adam Searleman,[1] Annette von Drygalski,[4] and Jiang Du[1]*

Purpose: To evaluate the echo dependence of 3D ultrashort echo time (TE) quantitative susceptibility mapping (3D UTE-QSM) and effective transverse relaxation rate (R_2^*) measurement in the setting of high concentrations of iron oxide nanoparticles.
Methods: A phantom study with iron concentrations ranging from 2 to 22 mM was performed using a 3D UTE Cones sequence. Simultaneous QSM processing with morphology-enabled dipole inversion (MEDI) and R_2^* single exponential fitting was conducted offline with the acquired 3D UTE data. The dependence of UTE-QSM and R_2^* on echo spacing (ΔTE) and first TE (TE_1) was investigated.
Results: A linear relationship was observed between UTE-QSM measurement and iron concentration up to 22 mM only, with the minimal TE_1 of 0.032 ms and ΔTE of less than 0.1 ms. A linear relationship was observed between R_2^* and iron concentration up to 22 mM only when TE_1 was less than 0.132 ms and ΔTE was less than 1.2 ms. UTE-QSM with MEDI processing showed strong dependence on ΔTE and TE_1, especially at high iron concentrations.
Conclusion: UTE-QSM is more sensitive than R_2^* measurement to TE selection. Both an ultrashort TE_1 and a small ΔTE are needed to achieve accurate QSM for high iron concentrations.
Magn Reson Med 79:2315–2322, 2018. © 2018 International Society for Magnetic Resonance in Medicine.

Key words: ultrashort echo time; Cones; QSM; R_2^*; high iron concentration

INTRODUCTION

Iron oxide nanoparticles (IONPs) have been increasingly used to generate MRI contrast for molecular imaging applications (1,2). The ability to accurately and noninvasively quantify IONPs is desirable for many emerging applications, including drug delivery (3–6), cell labeling and tracking (7–9), and magnetic fluid hyperthermia (10–12). In addition, endogenous iron, an essential cofactor for proteins with functions including oxygen delivery, mitochondrial respiration, and the inactivation of harmful oxygen radicals, can accumulate under pathological conditions (13–16). When systemic or local iron concentrations exceed the binding capacity of iron storage and transport proteins, the free iron will deposit into tissues. These iron deposits accelerate the production of free radicals, resulting in membrane lipid peroxidation, cellular injury, and ultimately organ dysfunction (17–20). For example, patients receiving frequent blood transfusions such as those with sickle cell anemia or thalassemia major can develop secondary hemochromatosis with resultant liver cirrhosis and heart failure (20,21), and patients with hemophilia can have repeated joint hemorrhage leading to focal iron deposition and subsequent joint deterioration (22). Noninvasively measuring endogenous iron deposits would be clinically useful in medical conditions associated with very high iron content, for instance, to monitor response to chelation therapy so that iron burden can be reduced while minimizing the risk of over chelation. Consequently, there is a growing interest in quantitative in vivo estimation of both endogenous and exogenous iron accumulation.

Iron is a paramagnetic transition metal that causes shortened T_1, T_2, and T_2^* relaxation times, as well as phase changes of nearby water protons, by its magnetic susceptibility effect (23–25). Because there is a linear increase in susceptibility with iron concentration, quantitative susceptibility mapping (QSM) MRI methods

[1]Department of Radiology, University of California, San Diego, California, USA.
[2]Institute of Electrical Engineering, Chinese Academy of Science, Beijing, China.
[3]Radiology Service, VA San Diego Healthcare System, San Diego, California, USA.
[4]Department of Medicine, Division of Hematology/Oncology, University of California, San Diego, California, USA.

Grant sponsor: Bioverativ, Human Resource and Service Agency (HRSA); Grant number: H30MC24045; Grant sponsor: National Institutes of Health (NIH); Grant numbers: R01AR062581-01A1, 1R01 NS092650, and T32EB005970; Grant sponsor: VA Clinical Science R&D Service; Grant number: merit award I01CX001388; Grant sponsor: National Natural Science Foundation of China (NSFC); Grant number: 51607169; Grant sponsor: Chinese Scholarship Council Grant (CSC); Grant number: 201504910174.

*Correspondence to: Jiang Du, PhD, University of California, San Diego, Department of Radiology, 200 West Arbor Drive, San Diego, CA 92103-8226. E-mail: jiangdu@ucsd.edu

Received 30 July 2017; revised 5 December 2017; accepted 5 December 2017
DOI 10.1002/mrm.27062
Published online 4 January 2018 in Wiley Online Library (wileyonlinelibrary.com).

have been developed to estimate iron accumulation in vivo (26–31). There are 2 widely used QSM-processing algorithms: the morphology-enabled dipole inversion (MEDI) (32,33) and improved sparse linear equation and least-squares (iLSQR) methods (34,35). These 2 methods and their extensions have shown success in quantifying tissue susceptibility with applications in brain (36,37), cartilage (with streaking artifact reduction (STAR) QSM), and cortical bone (with chemical shift QSM) (38,39).

Most QSM methods calculate the tissue-frequency shift using phase information at different echo times (TEs), and therefore are highly dependent on the accuracy of phase measurement. High iron concentrations can be particularly problematic because the high degree of T_2^* shortening leads to rapid signal decay with a low or no signal when using conventional clinical multiecho gradient recalled echo sequences. High iron concentrations also greatly increase the resonance frequency shift, which can cause severe phase wrapping beyond the capability of traditional phase unwrapping methods. As a result, QSM based on gradient recalled echo sequences with longer TEs (e.g., $TE > 2$ ms) may fail when evaluating high iron concentrations.

Ultrashort TE (UTE) sequences greatly reduce TE from the several milliseconds typically used in conventional clinical sequences down to tens of microseconds or less, allowing the direct detection of signals from short T_2 tissues such as cortical bone (40). UTE sequences have been used to measure the effective transverse relaxation rate ($R_2^* = 1/T_2^*$) of high IONP concentrations, and may be used to detect the associated fast phase evolution. The improvement in signal detection and phase measurement with UTE suggests that its combination with QSM (UTE-QSM) may allow for more accurate estimation of susceptibility when the T_2^* is greatly reduced by high iron concentrations. However, although originally believed to be TE-independent, recent literature has shown that QSM measurements can be highly TE-dependent (41). Therefore, it is of critical importance to understand the TE-dependence of UTE-QSM type sequences at high iron concentrations.

In this study, we aimed to investigate the capability and limitations of the UTE-QSM technique in evaluating high iron concentrations. A phantom study using different iron concentrations was carried out with a 3D UTE sequence combined with the MEDI method. The dependence of UTE-QSM and R_2^* measurement on TE was also investigated by using different combinations of echo spacing (ΔTE) and the first TE (TE_1).

METHODS

Phantom Preparation

Two sets of phantoms were prepared for this study. The first set was a gadolinium phantom, with diluted gadopentetate dimeglumine (Magnevist; Bayer HealthCare Pharmaceuticals, Wayne, NJ) in six 3 mL syringes in a cylindrical container (10 cm in diameter; height 30 cm) filled with agarose gel (0.9% by weight). The syringes contained 6 different concentrations of Magnevist: 1.5, 3, 4.5, 6, 7.5, and 9 mg/mL. The second set was an iron phantom which was composed of 3 mL syringes (1 cm diameter) filled with 2 mL of Feridex I.V. solution (ferumoxides injectable solution, Berlex Laboratories, Wayne, NJ) at 6 different concentrations: 2, 6, 10, 14, 18, and 22 mM. The syringes were put in a cylindrical container (10 cm in diameter; height 30 cm) filled with agarose gel (0.9% by weight). During MRI, the longitudinal direction of the syringes was parallel to the B_0 field to minimize susceptibility effects.

Pulse Sequences

MR imaging of the phantoms was performed on a 3T Signa HDxt scanner (GE Healthcare Technologies, Milwaukee, WI) using a previously reported 3D UTE Cones (3D UTE Cones) sequence (42–44). The basic 3D Cones sequence employed a short rectangular excitation pulse followed by 3D spiral trajectory k-space sampling with a conical view ordering. A transmit–receive quadrature coil (BC-10, Medspira, Minneapolis, MN) with a diameter of 22 cm was used for signal excitation and reception.

For the gadolinium phantom study, imaging parameters included matrix $= 128 \times 128 \times 100$, voxel size $= 1 \times 1 \times 1\,mm^3$, repetition time (TR)/TE = 30/3/4/5 ms, flip angle = 12°, bandwidth = 83.3 kHz, scan time = 5 min per scan.

For the iron phantom study, imaging parameters included acquisition matrix $= 200 \times 200 \times 60$, voxel size $= 0.4 \times 0.4 \times 0.5\,mm^3$, TR = 11.8 ms, flip angle = 18°, bandwidth = 62.5 kHz, and scan time = 4 min per scan. Initially, the linearity between R2* and iron concentration was examined using 12 TEs: 0.032, 0.132, 0.232, 0.332, 0.432, 0.632, 0.932, 1.232, 1.832, 2.432, 3.632, and 4.832 ms. Five sets of UTE acquisitions at evenly spaced TEs starting at TE_1 were used for UTE-QSM and R_2^* analyses of the echo combination datasets. To study the effect of ΔTE on UTE-QSM analysis, 5 different ΔTEs ($\Delta TE = 0.06$, 0.1, 0.3, 0.6, 1.2 ms) were investigated with TE_1 kept at a fixed value of 0.032 ms, leading to a total of 25 scans. To study the effect of TE_1, 6 different TE_1s ($TE_1 = 0.032$, 0.132, 0.232, 0.332, 0.632, 0.932 ms) were investigated with ΔTE kept at 0.1 ms, leading to a total of 30 scans.

Quantitative Susceptibility Mapping

Each 3D UTE Cones acquisition was reconstructed into both magnitude and phase images using a re-gridding algorithm, which interpolates the measured signal from Cones spokes onto a Cartesian grid. Nominal TEs were used for QSM calculation. Due to the nonuniform sampling density of our spiral trajectory, density compensation was applied to the measured signal prior to re-gridding. To form an echo combination dataset with specified ΔTE and TE_1, 5 single echo acquisitions with increasing TE were combined to form a 4D complex matrix.

The MEDI QSM reconstruction algorithm (32) was applied offline with the same complex matrix for measuring the susceptibilities from each of the different iron concentrations. The cylindrical phantom was masked, and the B_0 direction was calculated from localization information. The first three echoes of each dataset were used for estimating frequency shift in an iterative fashion. A region growing-based phase unwrapping algorithm (45) was

implemented to obtain the global frequency shift. The projection onto dipole fields algorithm was used to obtain the background-removed frequency shift and phase map. Dipole inversion of the local susceptibility distribution was achieved using an iterative Bayesian regulation method. For all datasets, the regularization parameter λ and radius for the spherical mean value operator were kept as 1000 and 5, respectively, for calculating magnetic susceptibility χ.

ROI Data Analysis and R_2^* Fitting

The relationship between QSM and R_2^* for different iron concentrations and different echo combinations was derived from user-defined regions of interest (ROIs). ROIs with fixed diameters of 1 cm were used to cover each tube. χ for each ROI was calculated using the MEDI algorithm. To study the stability of the QSM results for the different iron concentrations, averaged χ for each ROI of the different echo combinations was plotted. To study the linear relationship between the QSM results and different iron concentration, normalized QSM results (divided by χ for the 6 mM phantom, which was chosen arbitrarily) were plotted for each echo combination.

R_2^* values for each ROI were obtained using a Levenberg-Marquardt fitting algorithm developed in-house based on Equation [1]. A constant term C was introduced to account for background noise and artifacts associated with UTE data acquisition and image reconstruction.

$$S(TE) = s_0 \times e^{-R_2^* \times TE} + C. \quad [1]$$

R_2^* and UTE-QSM analysis algorithms were written in MatLab (MathWorks, Natick, MA) and were executed off-line on axial UTE images obtained with the protocols described above. The program allowed placement of ROIs on the first image of the series, which were then copied to the corresponding position on each of the subsequent images. The mean intensity within each of the ROIs was used for R_2^* curve fitting.

RESULTS

The gadolinium phantom study demonstrated an excellent linear relationship between UTE-QSM measurements and gadolinium concentrations (Supporting Fig. S1). Linear regression shows a R^2 of 0.9984, suggesting that the UTE-QSM sequence together with MEDI processing can reliably estimate susceptibility.

Figure 1 shows the R_2^* fitting results for the iron phantom study using UTE-QSM. The magnitude image of the phantom at the minimum TE is shown in Figure 1a, where the syringe with the lowest iron concentration demonstrates the highest signal intensity. Using 12 TEs ranging from 0.032 ms to 4.832 ms, a linear relationship was observed between R_2^* and iron concentration, as shown in Figure 1b, with a R^2 of 0.9983 and a slope of 0.194 ms^{-1}/mM. Figure 1c shows that iron concentrations below 18 mM are relatively linear over a range of ΔTE. However, the longest ΔTE at 1.2 ms overestimated the R_2^* at the highest iron concentrations of 18 and 22 mM. Interestingly, the R_2^*s of the lowest 2 iron concentrations were slightly overestimated with the shortest 2 ΔTEs of 0.06 and 0.1 ms. Figure 1d shows that R_2^* fitting is relatively linear for iron concentrations lower than 16 mM for all TE_1, but at iron concentrations above 16 mM the linear relationship becomes worse as TE_1 increases.

Figure 2 demonstrates how the QSM results depend on both iron concentration and ΔTE. Detailed results on UTE-QSM measurements for different IONP concentrations using different ΔTE and TE_1 are shown in Supporting Table S1. Figures 2a and 2b are the calculated phases after background removal and QSM results from MEDI using the projection onto dipole fields algorithm. QSM results were successfully obtained from the phase information. An obvious signal decay, as well as phase wrapping, can be observed at higher iron concentrations. Additional phase images are available in Supporting Figure S2. Figure 3 demonstrates that the QSM of iron concentrations below 6 mM remain stable for all the echo combinations with MEDI processing. A linear relationship exists between QSM value and iron concentration for ΔTE = 0.06 ms. However, the calculated QSM value of higher iron concentrations is increasingly underestimated as ΔTE increases.

Figure 4 shows the QSM results for echo combinations with different TE_1s. An obvious signal decay, as well as phase wrapping, can also be observed at higher iron concentrations in Figures 4a and 4b. Additional phase images are available in Supporting Figure S3. Figure 5 demonstrates that the QSM of iron concentrations below 10 mM are approximately linear for all tested TE_1s; however, the QSM values appeared to plateau at higher iron concentrations in a manner dependent on TE_1. Only the QSM values from the shortest TE_1 at 0.032 ms were approximately linear over all tested iron concentrations.

DISCUSSION

It is of great clinical significance to quantify endogenous and exogenous iron deposition in the human body. Clinical MRI sequences with conventional TE combinations are not able to accurately quantify iron overload (30). Sequences with much reduced TEs, such as UTE, zero TE, or sweep imaging with Fourier transformation- type sequences make it possible to accurately quantify iron overload (46–48). Nevertheless, these methods have limitations for accurate quantification in vivo because paramagnetic and diamagnetic substances are unable to be separated due to the positive-real nature of R_2^* or R_1 (31). By shortening the first TE with 3D radial UTE, QSM has been successfully applied for the study of ultrashort T_2^* tissues such as cortical bone (49). In this study, simultaneous QSM and R_2^* measurements were carried out to systematically investigate the capability of UTE-QSM sequences to quantify iron over a large dynamic range. Our results demonstrated that high iron concentrations will significantly reduce the signal decay time and induce dramatic phase wrapping within conventional TEs, leading to inaccurate R_2^* and MEDI-based QSM measurements. We found that QSM measurements were

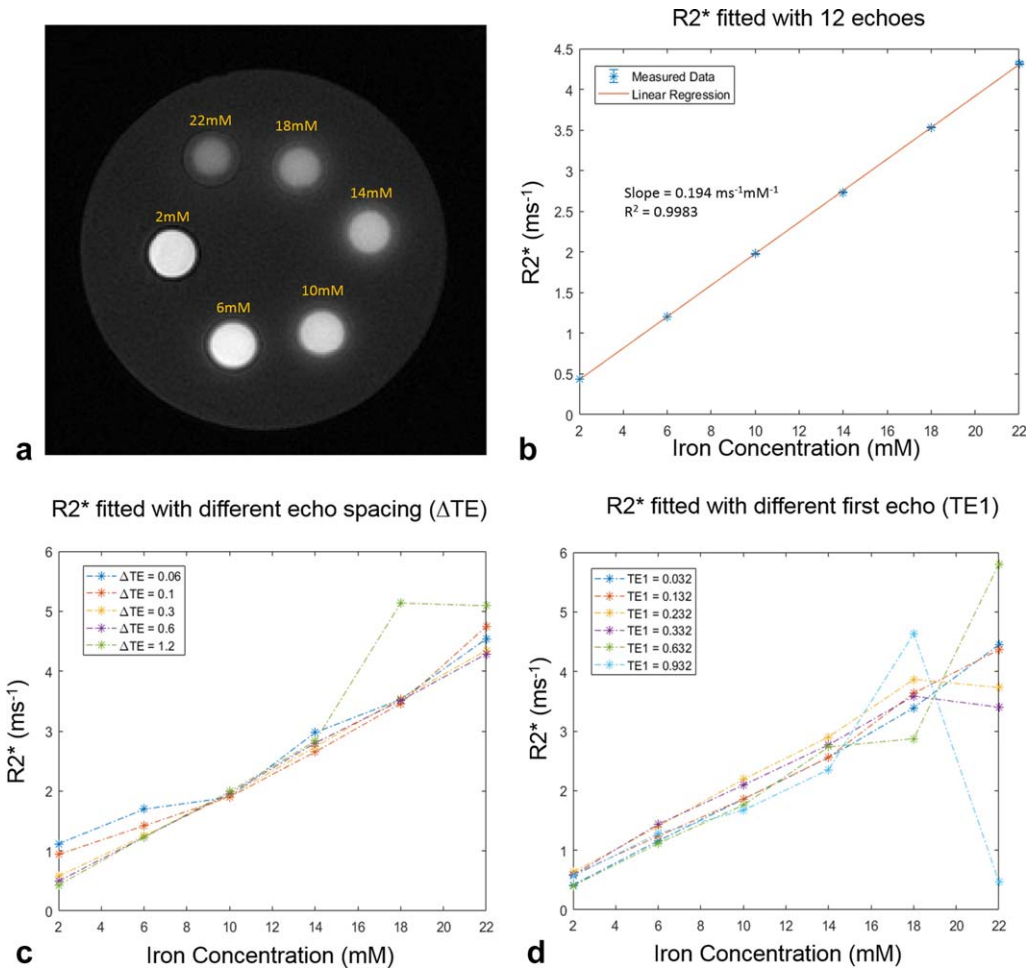

FIG. 1. (**a**) Phantoms with iron concentrations ranging from 2 to 22 mM are detected with high signal with the 3D ultrashort TE sequence using a TE of 0.032 ms. (**b**) A linear relation was observed between R_2^* and iron concentration using 12 TEs (0.032–4.832 ms). (**c**) Dependency of the apparent R_2^* of various iron concentrations on ΔTE, with TE_1 fixed at 0.032. (**d**) Dependency of the apparent R_2^* of various iron concentrations on the TE_1, with ΔTE fixed at 0.1 ms. ΔTE, echo spacing; R_2^*, effective transverse relaxation rate; TE = echo time; TE_1, first echo time.

only accurate over a large dynamic range of iron concentrations when the TE_1 was greatly reduced and the ΔTE was narrowed.

This study systematically investigated the dependency of MEDI-based QSM as well as R_2^* relaxometry on TE by compiling single-echo 3D UTE Cones acquisitions of a

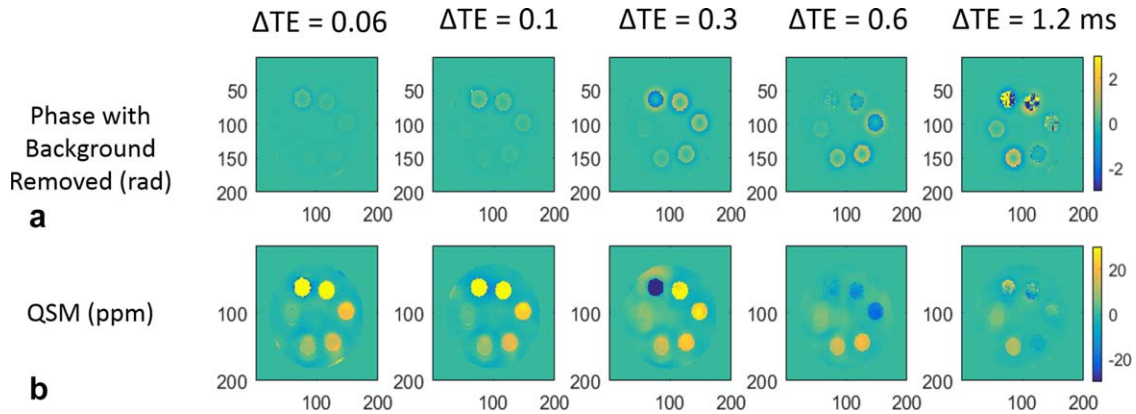

FIG. 2. QSM results of the iron phantom for different ΔTE, with TE_1 fixed at 0.032 ms. The (**a**) calculated phase (with background removed) and (**b**) QSM reconstructed with the morphology-enabled dipole inversion algorithm are shown. ΔTE, echo spacing; QSM, quantitative susceptibility mapping; TE_1 = first echo time.

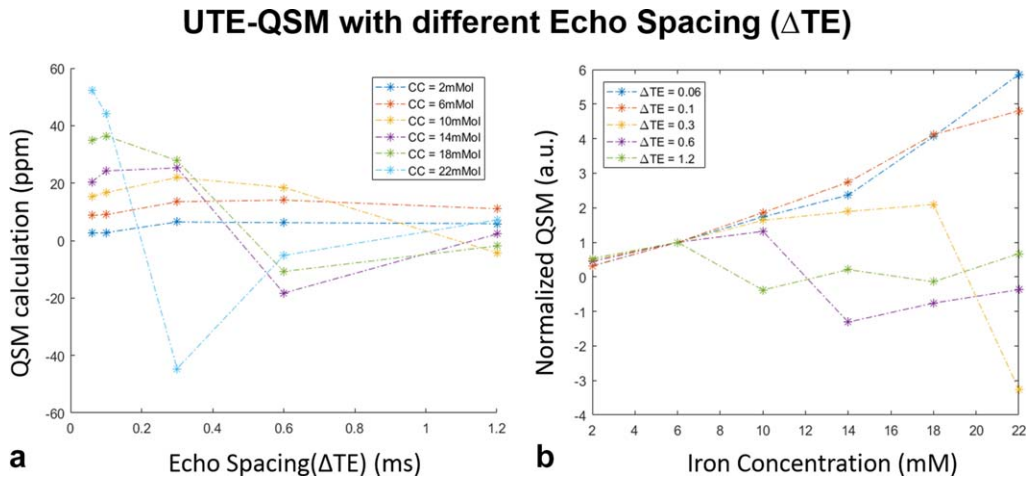

FIG. 3. QSM region-of-interest analysis depends on both CC and ΔTE. (**a**) MEDI-derived QSM values change with ΔTE dependent on the CC. (**b**) MEDI-derived QSM values at higher CC are more linear with short ΔTE. QSM values for each dataset were normalized by the QSM value at 6 mM iron. ΔTE, echo spacing; CC, iron concentration; MEDI, morphology-enabled dipole inversion; UTE-QSM, ultrashort echo time quantitative susceptibility mapping

phantom containing 6 different IONP concentrations into echo combination datasets. The echo combination datasets varied either by the first TE or by ΔTE interval. By comparing Figure 3b and Figure 5b, it can be concluded that a linear relationship between QSM and iron concentration only exists when TE_1 is reduced to 0.032 ms and ΔTE is less than 0.1 ms. The linear relationship gradually worsens for higher iron concentrations when TE_1 or ΔTE is increased. As might be expected, the R_2^* analysis was more dependent on the first TE than the ΔTE at high iron concentrations, reflecting the more severe reduction in initial signal magnitude. Our results are consistent with a recent study that showed QSM of bone could only be successfully obtained with reduced TE_1 and ΔTE (49). In contrast, another study using a TE_1 of 3 ms and ΔTE of 2 ms was unable to calculate bone susceptibility because bone signal was not detected (38). For clinical studies on iron overload, UTE with minimal nominal TEs and short ΔTE will be necessary for accurate QSM measurement, particularly in zones with highly concentrated iron.

Comparisons of MEDI- and iLSQR-based QSM, as well as other QSM methods, were not carried out in this study (50). The iLSQR algorithm may show different dependence on TE_1 and ΔTE than the MEDI algorithm, especially for higher iron concentrations. Sood et al. first reported that iLSQR-based QSM is dependent on TE selection, especially for different tissue properties (41). After a more systemic study, Cronin et al. concluded that phase-wrapping algorithms as well as tissue properties might be the main reasons for the TE dependence in iLSQR (51). In future studies, we will investigate the TE dependence in UTE-QSM with iLSQR processing, together with Laplacian unwrapping and other phase unwrapping algorithms.

A birdcage coil was used in this study for signal reception to avoid QSM reconstruction errors caused by phase combination. In practice, both the magnitude and phase images can be combined with an improved adaptive combined method when using multichannel coils (52).

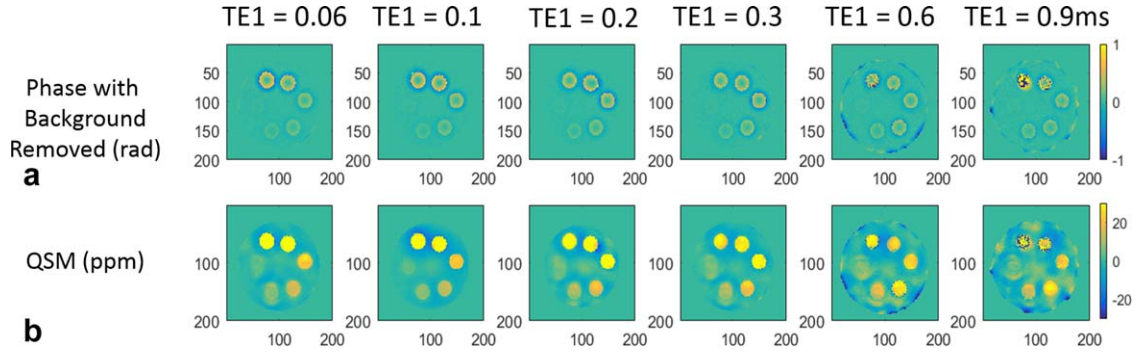

FIG. 4. QSM results of the iron phantom for different TE_1 with echo spacing fixed at 0.1 ms. The (**a**) calculated phase (with background removed) and (**b**) QSM reconstructed with the morphology-enabled dipole inversion algorithm are shown. TE_1, first echo time; QSM, quantitative susceptibility mapping.

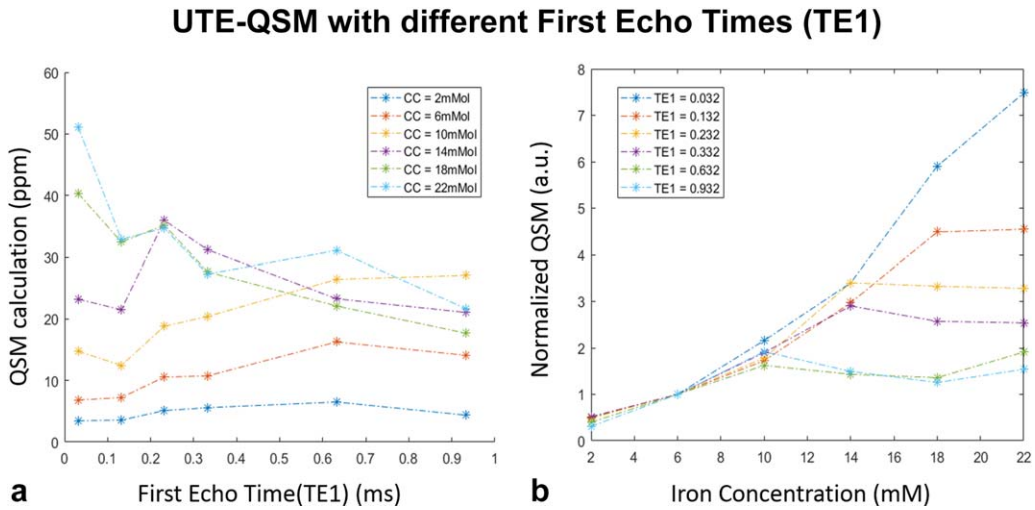

FIG. 5. QSM region of interest analysis depends on both CC and TE_1. (**a**) Morphology-enabled dipole inversion–derived QSM values change with TE_1 dependent on the CC. (**b**) QSM values are consistently underestimated by longer TE_1 as the CC increases. QSM values for each dataset were normalized by the QSM value at 6 mM iron. CC, iron concentration; TE_1, first echo time; UTE-QSM, ultrashort echo time quantitative susceptibility mapping.

This study has several limitations. First, IONPs of different concentrations were suspended homogeneously in our phantom. However, IONPs would be expected to accumulate or aggregate within biologic tissues, causing nonhomogeneous susceptibility values in vivo. Second, the chemical shift effect was not considered in this study. UTE-QSM, together with iterative decomposition of water and fat with echo asymmetry and least-squares emission (IDEAL) techniques, may help resolve potential issues. This study focuses on the measurable dynamic range changes with current QSM methods when combined with UTE sequences. The chemical shift effect is unlikely to affect the UTE-QSM results in this study. Third, the highest concentration of IONPs in this study was 22 mM, which is much lower when compared with 37.5 mM in a study of UTE T_2^* or T_1 measurement (46), and with 57.5 mM in a study using sweep imaging with Fourier transformation (47,48). As one of the main findings in this study, the QSM dynamic range is highly dependent on both the first TE and ΔTE. By further reducing ΔTE, even higher iron concentrations are expected to be accurately quantified at the cost of longer scan time. Parallel imaging or compressed sensing can be applied to reduce the scan time (53,54). Fourth, multiple single-echo 3D UTE Cones acquisitions were used for QSM study of high iron concentrations, which is more accurate but very time-consuming and inappropriate for clinical applications. Interleaved multiecho or echo-shifted 3D UTE Cones data acquisitions could be used for accurate QSM of both low and high iron concentrations, while greatly reducing the total scan time (55). Fifth, UTE-QSM with iLSQR processing was not conducted in this study. Because iLSQR and iLSQR-based susceptibility tensor imaging have shown greater robustness for long T_2 tissues, the TE_1 and ΔTE dependence of iLSQR using UTE-QSM at high iron concentrations would be interesting and will be investigated in the future.

CONCLUSION

Simultaneous QSM and R_2^* measurements of high iron concentration up to 22 mM were carried out based on 3D UTE Cones sequences. The effects of the first TE and ΔTE on the accuracy of QSM and R_2^* measurements were investigated on iron phantoms. QSM shows greater dependence on the first TE and ΔTE than R_2^*. UTE-QSM with MEDI processing shows a strong dependence on both ΔTE and the first TE, especially for high iron concentrations. Reasonable selection of ΔTE and the first TE will be important for future QSM studies of iron overload diseases.

ACKNOWLEDGMENTS

The authors acknowledge grant funding from Bioverativ, Human Resource and Service Agency (HRSA; H30MC24045), the National Institutes of Health (NIH; R01AR062581-01A1, 1R01 NS092650, and T32EB005970), VA Clinical Science R&D Service (Merit Award I01CX001388), National Natural Science Foundation of China (NSFC; 51607169), and Chinese Scholarship Council Grant (CSC; 201504910174).

REFERENCES

1. Gupta AK, Gupta M. Synthesis and surface engineering of iron oxide nanoparticles for biomedical applications. Biomaterials 2005;26:3995–4021.
2. Thorek DLJ, Chen AK, Czupryna J, Tsourkas A. Superparamagnetic iron oxide nanoparticle probes for molecular imaging. Ann Biomed Eng 2006;34:23–38.
3. Chertok B, Moffat BA, David AE, Yu F, Bergemann C, Ross BD, Yang VC. Iron oxide nanoparticles as a drug delivery vehicle for MRI monitored magnetic targeting of brain tumors. Biomaterials 2008;29:487–496.
4. Jain TK, Morales MA, Sahoo SK, Leslie-Pelecky DL, Labhasetwar V. Iron oxide nanoparticles for sustained delivery of anticancer agents. Mol Pharm 2005;2:194–205.
5. Marcu A, Pop S, Dumitrache F, et al. Magnetic iron oxide nanoparticles as drug delivery system in breast cancer. Appl Surf Sci 2013;281:60–65.

6. Wahajuddin, Arora S. Superparamagnetic iron oxide nanoparticles: magnetic nanoplatforms as drug carriers. Int J Nanomed 2012;7:3445–3471.
7. Li L, Jiang W, Luo K, Song H, Lan F, Wu Y, Gu Z. Superparamagnetic iron oxide nanoparticles as MRI contrast agents for non-invasive stem cell labeling and tracking. Theranostics 2013;3:595–615.
8. Barrow M, Taylor A, Murray P, Rosseinsky MJ, Adams DJ. Design considerations for the synthesis of polymer coated iron oxide nanoparticles for stem cell labelling and tracking using MRI. Chem Soc Rev 2015;44:6733–6748.
9. Rosen JE, Chan L, Shieh D-B, Gu FX. Iron oxide nanoparticles for targeted cancer imaging and diagnostics. Nanomedicine 2012;8:275–290.
10. Laurent S, Dutz S, Häfeli UO, Mahmoudi M. Magnetic fluid hyperthermia: focus on superparamagnetic iron oxide nanoparticles. Adv Colloid Interface Sci 2011;166:8–23.
11. Espinosa A, Di Corato R, Kolosnjaj-Tabi J, Flaud P, Pellegrino T, Wilhelm C. Duality of iron oxide nanoparticles in cancer therapy: amplification of heating efficiency by magnetic hyperthermia and photothermal bimodal treatment. ACS Nano 2016;10:2436–2446.
12. Blanco-Andujar C, Walter A, Cotin G, Bordeianu C, Mertz D, Felder-Flesch D, Begin-Colin S. Design of iron oxide-based nanoparticles for MRI and magnetic hyperthermia. Nanomedicine 2016;11:1889–1910.
13. Abbaspour N, Hurrell R, Kelishadi R. Review on iron and its importance for human health. J Res Med Sci 2014;19:164–174.
14. Sangani RG, Ghio AJ. Iron, human growth, and the global epidemic of obesity. Nutrients 2013;5:4231–4249.
15. Kohgo Y, Ikuta K, Ohtake T, Torimoto Y, Kato J. Body iron metabolism and pathophysiology of iron overload. Int J Hematol 2008;88:7–15.
16. Sharp PA. Intestinal iron absorption: regulation by dietary & systemic factors. Int J Vitam Nutr Res 2010;80:231–242.
17. Fleming RE, Ponka P. Iron overload in human disease. N Engl J Med 2012;366:348–359.
18. Siddique A, Kowdley K V. Review article: The iron overload syndromes. Aliment Pharmacol Ther 2012;35:876–893.
19. Murphy CJ, Oudit GY. Iron-overload cardiomyopathy: pathophysiology, diagnosis, and treatment. J Card Fail 2010;16:888–900.
20. Taher AT, Musallam KM, Inati A. Iron overload: consequences, assessment, and monitoring. Hemoglobin 2009;33(suppl 1):S46–S57.
21. Brittenham GM, Cohen AR, McLaren CE, Martin MB, Griffith PM, Nienhuis AW, Young NS, Allen CJ, Farrell DE, Harris JW. Hepatic iron stores and plasma ferritin concentration in patients with sickle cell anemia and thalassemia major. Am J Hematol 1993;42:81–85.
22. Roosendaal G, Vianen ME, Wenting MJ, van Rinsum AC, van den Berg HM, Lafeber FP, Bijlsma JW. Iron deposits and catabolic properties of synovial tissue from patients with haemophilia. J Bone Joint Surg Br 1998;80:540–545.
23. Rad AM, Arbab AS, Iskander AS, Jiang Q, Soltanian-Zadeh H. Quantification of superparamagnetic iron oxide (SPIO)-labeled cells using MRI. J Magn Reson Imaging 2007;26:366–374.
24. Kuhlpeter R, Dahnke H, Matuszewski L, Persigehl T, von Wallbrunn A, Allkemper T, Heindel WL, Schaeffter T, Bremer C. R2 and R2* mapping for sensing cell-bound superparamagnetic nanoparticles: in vitro and murine in vivo testing. Radiology 2007;245:449–457.
25. Girard OM, Ramirez R, McCarty S, Mattrey RF. Toward absolute quantification of iron oxide nanoparticles as well as cell internalized fraction using multiparametric MRI. Contrast Media Mol Imaging 2012;7:411–417.
26. Bilgic B, Pfefferbaum A, Rohlfing T, Sullivan EV, Adalsteinsson E. MRI estimates of brain iron concentration in normal aging using quantitative susceptibility mapping. Neuroimage 2012;59:2625–2635.
27. Wang Y, Liu T. Quantitative susceptibility mapping (QSM): decoding MRI data for a tissue magnetic biomarker. Magn Reson Med 2015;73:82–101.
28. Langkammer C, Schweser F, Krebs N, et al. Quantitative susceptibility mapping (QSM) as a means to measure brain iron?. A post mortem validation study. Neuroimage 2012;62:1593–1599.
29. Tan H, Liu T, Wu Y, et al. Evaluation of iron content in human cerebral cavernous malformation using quantitative susceptibility mapping. Invest Radiol 2014;49:498–504.
30. Sharma SD, Fischer R, Schoennagel BP, Nielsen P, Kooijman H, Yamamura J, Adam G, Bannas P, Hernando D, Reeder SB. MRI-based quantitative susceptibility mapping (QSM) and R2* mapping of liver iron overload: comparison with SQUID-based biomagnetic liver susceptometry. Magn Reson Med 2017;78:264–270.
31. Betts MJ, Acosta-Cabronero J, Cardenas-Blanco A, Nestor PJ, Düzel E. High-resolution characterisation of the aging brain using simultaneous quantitative susceptibility mapping (QSM) and R_2^* measurements at 7 T. Neuroimage 2016;138:43–63.
32. De Rochefort L, Liu T, Kressler B, Liu J, Spincemaille P, Lebon V, Wu J, Wang Y. Quantitative susceptibility map reconstruction from MR phase data using Bayesian regularization: validation and application to brain imaging. Magn Reson Med 2010;63:194–206.
33. Liu J, Liu T, de Rochefort L, et al. Morphology enabled dipole inversion for quantitative susceptibility mapping using structural consistency between the magnitude image and the susceptibility map. Neuroimage 2012;59:2560–2568.
34. Li W, Avram AV, Wu B, Xiao X, Liu C. Integrated Laplacian-based phase unwrapping and background phase removal for quantitative susceptibility mapping. NMR Biomed 2014;27:219–227.
35. Li W, Wang N, Yu F, Han H, Cao W, Romero R, Tantiwongkosi B, Duong TQ, Liu C. A method for estimating and removing streaking artifacts in quantitative susceptibility mapping. Neuroimage 2015;108:111–122.
36. Langkammer C, Liu T, Khalil M, Enzinger C, Jehna M, Fuchs S, Fazekas F, Wang Y, Ropele S. Quantitative susceptibility mapping in multiple sclerosis. Radiology 2013;267:551–559.
37. Wei H, Xie L, Dibb R, Li W, Decker K, Zhang Y, Johnson GA, Liu C. Imaging whole-brain cytoarchitecture of mouse with MRI-based quantitative susceptibility mapping. Neuroimage 2016;137:107–115.
38. Wei H, Dibb R, Decker K, Wang N, Zhang Y, Zong X, Lin W, Nissman DB, Liu C. Investigating magnetic susceptibility of human knee joint at 7 Tesla. Magn Reson Med 2017;78:1933–1943.
39. Dimov AV, Liu T, Spincemaille P, Ecanow JS, Tan H, Edelman RR, Wang Y. Joint estimation of chemical shift and quantitative susceptibility mapping (chemical QSM). Magn Reson Med 2015;73:2100–2110.
40. Du J, Carl M, Bydder M, Takahashi A, Chung CB, Bydder GM. Qualitative and quantitative ultrashort echo time (UTE) imaging of cortical bone. J Magn Reson 2010;207:304–311.
41. Sood S, Urriola J, Reutens D, O'Brien K, Bollmann S, Barth M, Vegh V. Echo time-dependent quantitative susceptibility mapping contains information on tissue properties. Magn Reson Med 2017;77:1946–1958.
42. Carl M, Bydder GM, Du J. UTE imaging with simultaneous water and fat signal suppression using a time-efficient multispoke inversion recovery pulse sequence. Magn Reson Med 2016;76:577–582.
43. Ma YJ, Zhu Y, Lu X, Carl M, Chang EY, Du J. Short T2 imaging using a 3D double adiabatic inversion recovery prepared ultrashort echo time cones (3D DIR-UTE-Cones) sequence. Magn Reson Med 2017. doi: 10.1002/mrm.26908.
44. Gurney PT, Hargreaves BA, Nishimura DG. Design and analysis of a practical 3D cones trajectory. Magn Reson Med 2006;55:575–582.
45. Cusack R, Papadakis N. New robust 3-D phase unwrapping algorithms: application to magnetic field mapping and undistorting echoplanar images. Neuroimage 2002;16:754–764.
46. Hong W, He Q, Fan S, Carl M, Shao H, Chen J, Chang EY, Du J. Imaging and quantification of iron-oxide nanoparticles (IONP) using MP-RAGE and UTE based sequences. Magn Reson Med 2017;78:226–232.
47. Wang L, Tang W, Zhen Z, Chen H, Xie J, Zhao Q. Improving detection specificity of iron oxide nanoparticles (IONPs) using the SWIFT sequence with long T2 suppression. Magn Reson Med 2014;32:671–678.
48. Zhang J, Chamberlain R, Etheridge M, Idiyatullin D, Corum C, Bischof J, Garwood M. Quantifying iron-oxide nanoparticles at high concentration based on longitudinal relaxation using a three-dimensional SWIFT look-locker sequence. Magn Reson Med 2014;71:1982–1988.
49. Dimov AV, Liu Z, Spincemaille P, Prince MR, Du J, Wang Y. Bone quantitative susceptibility mapping using a chemical species-specific R2* signal model with ultrashort and conventional echo data. Magn Reson Med 2018;79:121–128.
50. Langkammer C, Schweser F, Shmueli K, et al. Quantitative susceptibility mapping: report from the 2016 reconstruction challenge. Magn Reson Med 2018;79:1661–1673.

51. Cronin MJ, Wang N, Decker KS, Wei H, Zhu W-Z, Liu C. Exploring the origins of TE-dependent QSM measurements in healthy tissue and cerebral microbleeds. Neuroimage 2017;149:98–113.
52. Ma Y-J, Liu W, Zhao X, Tang W, Zhang Z, Tang X, Fan Y, Li H, Gao J-H. Improved adaptive reconstruction of multichannel MR images. Med Phys 2015;42:637–644.
53. Ma YJ, Liu W, Tang X, Gao JH. Improved SENSE imaging using accurate coil sensitivity maps generated by a global magnitude-phase fitting method. Magn Reson Med 2015;74:217–224.
54. Lustig M, Donoho D, Pauly JM. Sparse MRI: the application of compressed sensing for rapid MR imaging. Magn Reson Med 2007;58: 1182–1195.
55. Ma YJ, Liu W, Zhao X, Tang W, Li H, Fan Y, Tang X, Zhang Y, Gao JH. 3D interslab echo—shifted FLASH sequence for susceptibility weighted imaging. Magn Reson Med 2016;76:222–228.

SUPPORTING INFORMATION

Additional supporting information may be found in the online version of this article.

Table S1. UTE-QSM with MEDI processing for different IONPs concentrations using five different ΔTEs ranging from 0.06 to 1.2 ms and six different TE1s ranging from 0.032 to 0.932 ms.

Fig. S1. Phantom experimental validation of the UTE-QSM sequence with MEDI processing: (a) susceptibility map in ppm of six different Gd concentrations: 1.5, 3, 4.5, 6, 7.5, and 9 mg/ml, and (b) linear regression plot of UTE-QSM measurement by Gd concentration.

Fig. S2. Phase map (rad) of the iron phantom at each TE in the variable echo spacing dataset. The echo spacing (ΔTE) changes as shown by the row headings. The first TE was fixed at 0.032 ms.

Fig. S3. Phase map (rad) of the iron phantom at each TE in the variable first echo time dataset. The first echo time (TE1) changes as shown by the row headings. Echo spacing was fixed at 0.1 ms.